

Boise State University

ScholarWorks

---

Electrical and Computer Engineering Faculty  
Publications and Presentations

Department of Electrical and Computer  
Engineering

---

7-2021

## Effects of Memristive Synapse Radiation Interactions on Learning in Spiking Neural Networks

Sumedha Gandharava Dahl  
*Boise State University*

Robert C. Ivans  
*Boise State University*

Kurtis D. Cantley  
*Boise State University*

---


### Publication Information

Gandharava Dahl, Sumedha; Ivans, Robert C.; and Cantley, Kurtis D. (2021). "Effects of Memristive Synapse Radiation Interactions on Learning in Spiking Neural Networks". *SN Applied Sciences*, 3, 555.  
<https://doi.org/10.1007/s42452-021-04553-0>



# Effects of memristive synapse radiation interactions on learning in spiking neural networks

Sumedha Gandharava Dahl<sup>1</sup> · Robert C. Ivans<sup>1</sup> · Kurtis D. Cantley<sup>1</sup> 

Received: 26 September 2020 / Accepted: 1 April 2021 / Published online: 13 April 2021  
© The Author(s) 2021 

## Abstract

This study uses advanced modeling and simulation to explore the effects of external events such as radiation interactions on the synaptic devices in an electronic spiking neural network. Specifically, the networks are trained using the spike-timing-dependent plasticity (STDP) learning rule to recognize spatio-temporal patterns (STPs) representing 25 and 100-pixel characters. Memristive synapses based on a  $\text{TiO}_2$  non-linear drift model designed in Verilog-A are utilized, with STDP learning behavior achieved through bi-phasic pre- and post-synaptic action potentials. The models are modified to include experimentally observed state-altering and ionizing radiation effects on the device. It is found that radiation interactions tend to make the connection between afferents stronger by increasing the conductance of synapses overall, subsequently distorting the STDP learning curve. In the absence of consistent STPs, these effects accumulate over time and make the synaptic weight evolutions unstable. With STPs at lower flux intensities, the network can recover and relearn with constant training. However, higher flux can overwhelm the leaky integrate-and-fire post-synaptic neuron circuits and reduce stability of the network.

**Keywords** Neuromorphic circuits · Non-linear memristor model · Radiation · Spike-timing-dependent plasticity (STDP) · Leaky integrate-and-fire (LIF) neuron · Spatio-temporal pattern learning

## 1 Highlights

- Interactions between memristive synapses and radiation alters the spike-timing-dependent plasticity (STDP) learning mechanism.
- Without presentation of spatio-temporal patterns (training), radiation effects build up and destabilize the spiking neural network.
- Constant network training with spatio-temporal patterns overcomes radiation effects at low flux, but not at higher flux intensities.

## 2 Introduction

Artificial neural networks (ANNs) are densely connected computing systems inspired by the topology of biological neural networks. ANNs are adept at processing massive amounts of information in parallel and have the ability to derive meaning from complicated or imprecise data by recognizing complex patterns and trends. Trained ANNs are able to perform visual recognition [1], character recognition [2], voice-activated assistance [3], stock market forecasting [4], and are used in self-driving cars [5]. Industry pioneers are designing ANNs that can also be used in solar radiation forecasting, object classification and matching, event filtering, facial recognition, combat automation, target identification and weapon optimization

✉ Kurtis D. Cantley, [kurtiscantley@boisestate.edu](mailto:kurtiscantley@boisestate.edu) | <sup>1</sup>Department of Electrical and Computer Engineering, Boise State University, Boise, ID 83725, USA.



[6]–[8]. The next generation of systems are expected to be even more deeply biologically inspired, using pulses or spikes to transfer data between elements as opposed to continuous variables and activation functions. Customized hardware implementations will enable these spiking neural networks (SNNs) to be not only highly efficient but also incredibly robust and fault-tolerant. As such, they may find numerous applications in harsh, radiation-filled environments such as space or at nuclear and military installations. Practical examples include deployment of autonomous robots for nuclear waste handling, nuclear reactor maintenance, or space vehicle repair that contain onboard video processing, simultaneous localization and mapping (SLAM), and integration with numerous other sensing systems. For the sake of creating robust designs in the future, it is critical to understand just how resilient these electronic SNNs can be when subjected to disturbances from ionizing radiation.

While shielding and hardening are common practice to protect devices and circuits from radiation, these techniques are unable to block all particles from interacting with underlying electronics [9, 10]. This article aims to analyze the effect of radiation on the spatio-temporal pattern recognition (STPR) capability of SNNs with memristive synapses. At present, there are no known studies in the literature using modeling and simulation to investigate SNN radiation effects at the network level. However, the spike timing-dependent plasticity (STDP) learning mechanism and corresponding network training approaches have been broadly employed. For simplicity, biphasic shaping of the action potential pulses is used to realize STDP [11, 12], and STPR is achieved through repetitive presentation of correlated pattern windows [13, 14].

Although network-level investigations are limited, there are numerous reports detailing the effect of radiation on memristive devices themselves. Section 2 of this paper discusses various types of memristors, their use in spiking neural networks, and provides an overview of how radiation affects memristive devices with appropriate citations. Section 3 then details the experimental methodologies employed in this study, starting with the neural network topology and the components used and followed by a description of the modified memristor model that includes radiation effects. Specifically, a modified non-linear memristor drift model is used to induce effects of radiation in the circuit. Section 4 shows the simulation results and discusses subsequent analysis approaches. The memristor model is verified with and without radiation, and the effect of initial state and radiation on the STDP learning curve are presented. Networks with 5, 25, and 100 neurons are simulated to observe the effect of radiation at a different intensity, flux, and period. Changes in network learning capability and system stability are statistically

analyzed. Although networks with only one or a few output neurons and two layers are not generally useful, the results are broadly relevant. For example, these results can provide insight into the operation and response of filters within hidden layers of deep convolutional neural networks to radiation [15]. Section 5 concludes the paper, with the primary result being that when the network is not undergoing training, the effects of radiation build up as the deposited energy is not dissipated and the network becomes less stable. On the other hand, it is likely possible for the network to overcome larger amounts of radiation exposure when undergoing continuous on-line training or periodic re-training.

## 3 Background

The concepts, components, and terminologies regarding the neural networks and models used throughout the remainder of the paper are given in this section. Types of memristors, SNNs, and an overview of experimental radiation effects on memristors from the literature are provided.

### 3.1 Memristors

Memristors are two-terminal devices that will change resistance state when a sufficient external bias is applied as dictated by their physical properties. Memristors can also hold their resistance state in the absence of an external active source. The electrical properties of a memristor depend on the physical mechanism or resistance switching, which could be due to metal ions forming a conductive bridge (CBRAM), movement of oxygen ions (RRAM), phase change of the active material (PCM) or self-directed channel (SDC) [16]. PCM memristors usually acquire only two states, one of high resistance (RESET or *off-state*) and another of low resistance (SET or *on-state*). This property enables PCM devices to be used as a digital memory element. On the other hand, SDC and CBRAM memristors can reliably acquire multiple intermediate states and this property make them a viable candidate as synapses in electronic SNNs [16]. Essentially all memristor designs can be densely integrated into crossbar or cross-point architectures [17, 18]. Although disadvantages to this approach sometimes exist (such as sneak path currents), they are overall a promising candidate specific SNN implementations.

### 3.2 Spiking neural networks (SNNs)

Compared to most ANNs, SNNs are more biologically realistic and potentially powerful. They are designed using spiking neurons that transfer information via precise

timing or sequences of neural action potentials [19]. Neurons in biological neural networks are electrically excitable and communicate with each other by electrochemical signaling via synaptic connections. The strength of the connections between biological neurons is referred to as the synaptic weight, which changes over time depending on the pre- and post-synaptic neuron activity. Spike-timing-dependent plasticity (STDP) is one biological process that alters the weight depending on pre- and post-synaptic neuron firing time. One way to implement STDP in electronic SNNs is to modify the time, shape, and magnitude of the action potentials in the appropriate manner.

### 3.2.1 Software-based spiking neural networks

In software-based SNNs, weight change, topology, and learning are defined using software algorithms implemented using a digital, or von Neumann architecture. Time differences between pre- and post-synaptic neurons are detected and synaptic weights are modified accordingly using the STDP rule. Many multi-layer SNN algorithms have been successfully implemented in software to solve practical problems like speech recognition [20], face recognition [21], handwriting recognition [22] and robot control [23].

Software-based SNNs lead to the tradeoff among accuracy, memory, and processing speed. The need for non-volatile synaptic weight storage becomes a concern as continuous updates and fetch-decode-execute cycles require significant power consumption. Another concern is the implementation of multilayer networks that need readout of synaptic weights in each epoch. These are complicated to implement and add mismatches and communication errors into the network [24–26].

### 3.2.2 Hardware-based electronic neural networks

On the other hand, the physical realization of synapses using memristors are becoming a reality as they have the potential to solve many of the above-mentioned issues [27, 28]. Most memristors are non-volatile and do not lose their state, thus eliminating the need for readout of synaptic weights and reducing communication overhead across the network. Unlike other non-volatile memories, memristors do not need to be refreshed to maintain their state, and this decreases the power consumption of the system. Hardware implementation of SNNs will not require complex algorithms and their scalability will solve the issue of chip area [26].

## 3.3 Radiation effects on memristors

The literature contains many experimental radiation studies done on memristive devices with different active

materials, stack configurations, and physical modes of operation [29–34]. Such radiation studies have an enormous number of variables such as radiation source energy and exposure trajectory, the thickness of active and other layers, and device shielding and packaging techniques used. Thus, the results vary considerably and make cumulative studies inconclusive. However, some characteristic device changes are predominantly noted, including how radiation interaction events can change the present resistive state (state-altering radiation), induce  $e^-h^+$  pair current (ionizing radiation), and alter the *off*-state resistance of the device (typically observed as long-term degradation of  $R_{off}$ ).

A state-altering radiation event will change the present conductive state of the device. Such radiation effects have been experimentally observed in  $TiO_2$  devices following alpha and proton irradiation, resulting in more current through the device [29, 30]. No detectable change in *on* and *off* resistance of the device was reported after radiation. Similar state altering effects were also noted in [31] due to proton irradiation. The memristive device can be ionized by Gamma rays and high energy Bi ions, generating multiple  $e^-h^+$  pairs in the device thus increasing current [30]. However, no change in *on* and *off* resistance of the device was observed in either of the cases. Similar ionization effects were also experimentally observed in ref. [35]. Change in *off*-state resistance of the device is experimentally observed when the chalcogenide phase change devices were exposed to gamma and electron radiation [36]. Such radiation potentially decreases the read-window of the device and increases the leakage current due to new defects as observed in Cu filament based ReRAM devices following proton exposure [37]. Refs. [35, 38] also show changes in  $R_{off}$  because of silicon ion and alpha irradiation. The wide variation in these results make it infeasible to model extremely specific situations in larger circuits and necessitate a more general approach that points toward broader conclusions.

## 4 Experimental approach

This section details the configuration of two networks used for simulations in this work and their components and associated behavioral models. It also describes the modified memristor model used to include radiation interactions. Radiation profiles are quantified at the end to provide a comparison with experimental studies.

### 4.1 Neural network topology

Neural networks in this study have three basic components: pre-synaptic neurons, post-synaptic neurons, and

memristive synapses connecting afferents to the output layer. This study uses two types of network topologies. The first is shown in Fig. 1a and represents a fully connected network in which all three pre-synaptic neurons ( $N_1$ ,  $N_2$ , and  $N_3$ ) are electrically connected to two post-synaptic neurons ( $N_4$  and  $N_5$ ) via five memristors ( $M_1$  to  $M_5$ ). This network only uses square digital pulses as the action potentials. The second topology is represented by a spiking neural network in Fig. 1b is a single layer perceptron network with either 25 or 100 pre-synaptic afferents ( $N_1$  to  $N_{25 \text{ or } 100}$ ), each connected to a single post-synaptic neuron (LIF post N) via single memristors ( $M_1$  to  $M_{25 \text{ or } 100}$ ).

The post-synaptic neuron in the biphasic spiking neural network of Fig. 1b is designed in Verilog-A representing a leaky integrate-and-fire (LIF) circuit behavior governed by Hodgkin-Huxley equations. The LIF circuit fires a bi-directional biphasic spike (toward the dendritic and axonic synapses) when a certain threshold is reached. Both networks follow STDP learning where the conductivity of the memristive synapse (the connection between two neurons) is modified interdependently due to the presence of pre- and post-synaptic pulses. For simulation purposes, dependent voltage supplies are used to mimic neuron behavior in  $N_1$  to  $N_{5/25/100}$ .

## 4.2 Non-linear drift memristor model

As discussed in Sect. 2.1, researchers have developed memristors using numerous types of materials and working mechanisms. A wide variety of memristor models are present in literature to mimic a range of behaviors [39–41]. Mathematical models have many parameters to choose from and represent their respective device characteristics very closely, but their accuracy is limited since input parameters need to be modified for each given shape

and frequency of the input [39, 42, 43]. A physical model called a non-linear memristor drift model by Chua et al. [26] is used in this work and is motivated by  $\text{TiO}_2$  memristive devices. Depiction of the  $\text{TiO}_2$  memristive device is presented in Fig. 2a where  $\text{TiO}_2$  insulator layer of thickness  $D$  (presented by resistance  $R_{\text{off}}$ ) is between two conductive top and bottom electrodes. As potential is applied across the device, oxygen vacancies are created resulting in the formation of a conducting channel of width  $w$ . As the width  $w$  of this channel varies, the state and conductivity of the device also changes. Thus, the device sees a change in the magnitude of the current flowing through it at a given voltage. The model uses a window function represented by the auxiliary circuit in Fig. 2b to capture the non-linearity presented by memristive devices while using the physical characteristics of the device. Figure 2b (grey area) is the electrical representation of the behavioral model that includes the main circuit with  $E_{\text{mem}}$  (dependent voltage source) and  $R_{\text{off}}$  (Off resistance of device) and auxiliary circuit with dependent current source ( $G_x$ ), 1 F capacitor ( $C_x$ ) and window function  $f(x)$ . More details about model physics, implementation in Verilog-A and parameter used can be found in ref. [44]. The ratio  $w/D$  is called a state variable and is a unitless representation of the conductivity of the device at any given time. The ratio  $w/D$  is bounded between zero (very resistive,  $R_{\text{mem}} = R_{\text{off}}$ ) and one (very conductive,  $R_{\text{mem}} = R_{\text{on}}$ ). Parameters used in the model are  $R_{\text{on}} = 1 \text{ k}\Omega$ ,  $R_{\text{off}} = 100 \text{ k}\Omega$ ,  $\mu = 10 \text{ fm}^2/\text{V}$  and  $D = 10 \text{ nm}$ , so as to mimic the characteristics of HP Labs memristor.

## 4.3 Memristor model with radiation

The non-linear memristor drift model is modified to include the widely observed effects of radiation including

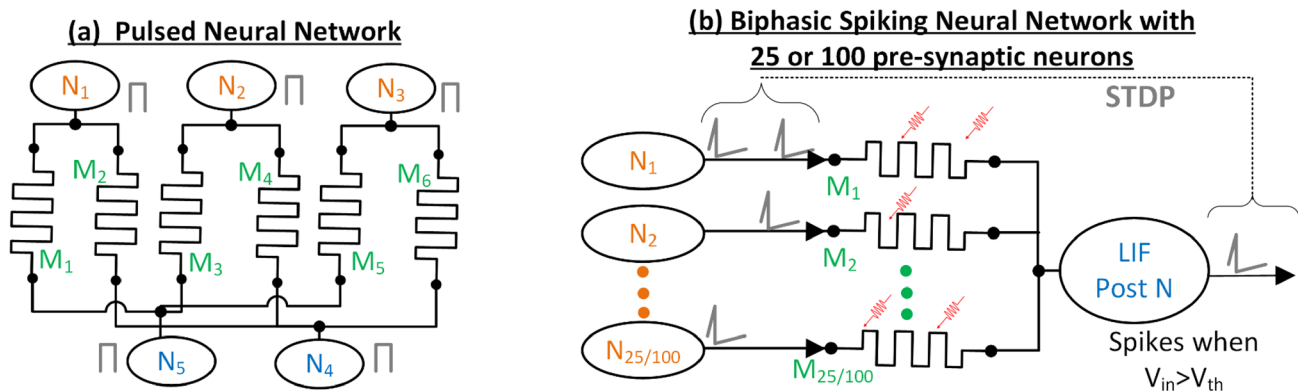


**Fig. 1** Memristor-based electronic SNNs used in this study. **a** Three pre-synaptic neurons each connected to two post-synaptic neurons via memristors used as synapses. This network uses randomly occurring digital square pulses to modify the synaptic weights. **b**

25 or 100 pre-synaptic neurons are connected to one post-synaptic leaky integrate-and-fire (LIF) neuron via single memristors. The network uses bi-phasic shaped pulses to achieve pair-based STDP for pattern learning



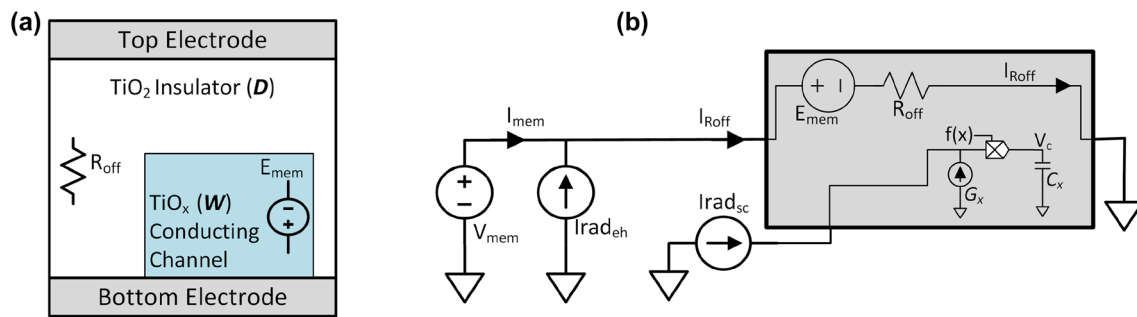


**Fig. 2** **a** TiO<sub>2</sub> RRAM. The TiO<sub>2</sub> insulator layer of thickness  $D$  ( $R_{off}$ ) is between two conductive electrodes. Presence of oxygen vacancies resulted in the formation of varying conducting channel of width  $w$  as  $E_{mem}$  in model. **b** Non-linear drift memristor model implemented in Cadence Virtuoso Specter using Verilog-A. The grey box represents the memristor behavioral model including the auxil-

iary circuit that controls voltage source  $E_{mem}$  in the main circuit. State-altering radiation ( $I_{rad_{sc}}$ ) is added to the auxiliary circuit to modify the state of device instantaneously and Ionizing radiation ( $I_{rad_{eh}}$ ) is induced in the circuit such that it adds to the memristor current ( $I_{mem}$ ) without affecting the memristor state directly

state-alteration, ionization, and *off*-state resistance change discussed in Sect. 2.3. State-altering radiation and ionizing radiation is induced in the circuit using current sources  $I_{rad_{sc}}$  and  $I_{rad_{eh}}$ . The state-altering radiation current source adds charge directly to the auxiliary circuit thus effectively changing the state of the device as needed. On the other hand, the ionizing radiation current is added to the memristor circuit current ( $I_{mem}$ ) and does not modify the state variable directly. The resulting full schematic is shown in Fig. 2b. In the absence of radiation, the model reverts to the non-linear memristor drift model. Model parameters can be modified to mimic the behavior of different types of memristors making it essentially agnostic to the type of materials used in the memristive device. Current sources mimicking the radiation behavior provide the correct observable response as noted in the literature and can be modified to expected energy source thus the model is also agnostic to an exact source of radiation. Further details about the model can be found in [44].

#### 4.4 Quantifying radiation

Current sources  $I_{rad_{sc}}$  and  $I_{rad_{eh}}$  artificially induce radiation in the circuit using pulses of 1 ms duration. Current pulse train magnitude follows a random Gaussian distribution with mean  $\mu$  and standard deviation  $\sigma$ , and time intervals follow a Poisson process similar to radiation patterns observed in real sources. In the model, one current pulse does not necessarily represent one radiation particle or interaction event.

In the literature, experimental studies using memristors have observed 30% [34], 77% [29, 32], 90% [45], and 95% [31] change in resistance (from *off*-state) when bombarded with radiation of a total fluence of  $7.7 \times 10^{15}$  350-keV proton/cm<sup>2</sup>,  $1.4 \times 10^{11}$  1-meV alpha/cm<sup>2</sup>,  $4.9 \times 10^{12}$  14.1-meV neutrons/cm<sup>2</sup>, and  $7.75 \times 10^{16}$  10-keV x-rays/

cm<sup>2</sup> respectively. Similar changes can be induced in the designed memristor model when 10, 20, 25, and 30  $I_{rad_{sc}}$  current pulses of magnitude  $\mu = 25 \mu A$  and  $\sigma = 12.5 \mu A$  are applied. Thus, model results are comparable to the experimental studies performed in the TiO<sub>2</sub> memristors. For this work, simulation of the networks is performed at different radiation flux or intensity, obtained by modifying the pulse interval (following a random Poisson distribution) and magnitude [44]. Synaptic weight change ( $\Delta w/D$ ) of memristive synapses increases as the mean magnitude and frequency (flux) of state-altering radiation current increases. Flux calculations in the study are based on an assumed 100 nm  $\times$  100 nm interaction size for the memristive devices.

A physical non-linear memristor drift model used in this study is used in well-read publications such as Chua et al. [26], Strukov et al. in 2008 [46], and Jogelkar and Wolf [47]. The memristor model is modified to include radiation effects. The radiation model is designed and implemented such that model results are comparable to the experimental studies performed in the TiO<sub>2</sub> memristors [29, 31, 32, 34, 45]. The published work on radiation effects on spiking neural network implementations is extremely limited. There are radiation studies on specific device technologies and more traditional architectures like CMOS structures at multiple technology nodes [48]–[50], MOS oxide [51, 52], rectifier circuits [53] and diodes [54].

#### 5 Simulation results and analysis

The following section presents the characteristics of the memristor (Fig. 1) model and its behavior in the presence of radiation. The effect of initial memristor state and radiation on the STDP learning curve are also presented, followed by network response to radiation in the absence of

patterns. Finally, the effect on the spatio-temporal pattern learning ability of the networks (Fig. 1) in the presence of radiation of different flux, duration, and intensity is examined. All the following simulations are performed using the Spectre transient simulation tool in the Cadence Virtuoso design suite.

### 5.1 Memristor model characteristics

Figure 3 shows the electrical characteristics of the memristor model. To analyze the non-linearity in the device, a train of  $125 + 1$  V pulses followed with  $125 - 1$  V pulses are applied with a pulse period (PP) of 1 ms and a pulse width (PW) of 0.9 ms. Figure 3a, b plot the conductivity and synaptic weight ( $w/D$ ) of the memristor versus pulse count and device current, respectively. Non-linearity is obvious in Fig. 3a when the device reaches off-state (lowest conductivity) and the slight change is linearity of  $w/D$  is also present as the device reaches the on-state (highest conductivity). The similar pattern can be observed in Fig. 3b where a logarithmic change in conductance versus current is almost linear, representing a logarithmic change in conductance with device current.

Figure 3c, d show the current–voltage characteristic of the device when 0.6 V sinusoidal and triangular periodic voltage is applied to the memristive device at varying frequency (respectively). At higher device threshold of 0.5 V in Fig. 3d, the memristor could not change the state completely as the frequency increases. At lower threshold of 0.25 V in Fig. 3c, the device switches state completely before reaching the threshold at higher frequencies. Figure 3c, d also shows the stability of model at different resistance state. Note the I-V curve displays a pinched hysteresis loop and the hysteresis lobe area decreases as input frequency increases, finally reducing to a line at a higher frequency. These are necessary characteristics of the I-V curve of a memristive device [55]. More model verification characteristics can be found in [44].

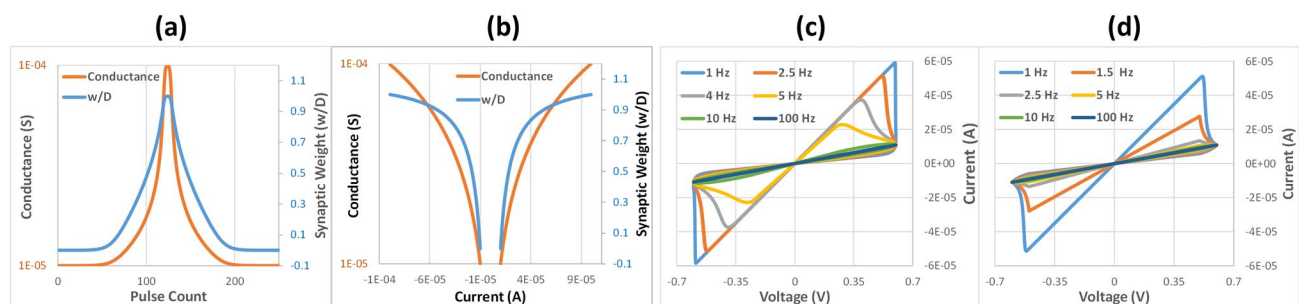


**Fig. 3** The memristor device shows a non-linear change in conductance and synaptic weight ( $w/D$ ) when a train of  $125 + 1$  V pulses followed with  $125 - 1$  V are applied (PW=0.9 ms, PP=1 ms). **a** Conductance and  $w/D$  versus pulse count and **b** versus device

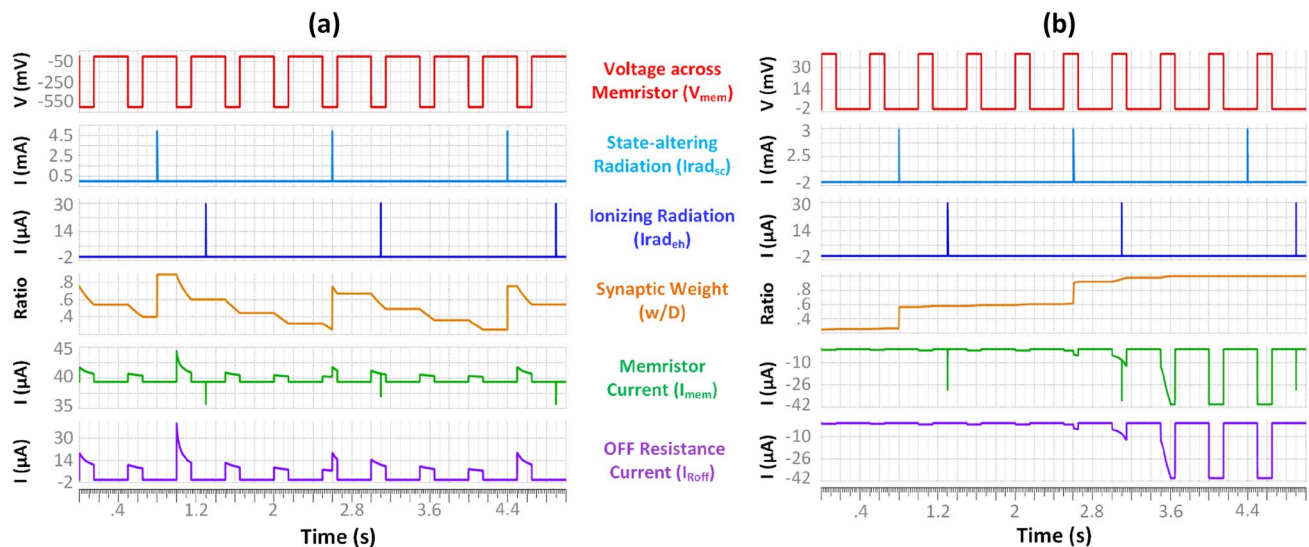
### 5.2 Verifying memristor radiation model

Figure 4 shows the changes in the synaptic weight ( $w/D$ ), device current ( $I_{\text{Roff}}$ ) and circuit current ( $I_{\text{mem}}$ ) in a transient simulation as state-altering ( $I_{\text{rad}_{sc}}$ ) and ionizing ( $I_{\text{rad}_{eh}}$ ) radiation is induced in the circuit in form of current pulses. In Fig. 4a, a pulse train of  $-0.5$  V is applied due to which synaptic weight ( $w/D$ ) and thus conductivity is decreasing. As 5 mA (1 ms) state-altering radiation spike is presented synaptic weight suddenly increases leading to an undesirable increase in device conductivity followed by an increase in device and circuit current. On the contrary, when ionizing radiation pulse arrives,  $I_{\text{mem}}$  sees the decrease in the current to compensate but device current ( $I_{\text{Roff}}$ ) and  $w/D$  are not affected. Similar results are experimentally recorded in [29] where no detectable effect of ionization is observed after the event. Figure 4b shows similar effects of radiation on the device even when input is a pulse train of 40 mV (positing pulse) resulting in increased  $w/D$ . More effects of radiation events on model characteristics can be found in ref. [44].

### 5.3 Pair-based STDP curves

As mentioned in Sect. 2.2, STDP is a biological process that changes the strength of the connection based on pre- and post-synaptic neuron firing time. STDP is also deemed responsible for brains ability to form memories, locate sounds and respond to threats and many shapes of STDP are biologically observed in different areas of brains in different species [56, 57]. In memristive devices, different shape of pre- and post-synaptic neuron spike can be used to obtain the desired STDP shape [12, 58]. Often, a simple pair-based STDP implementation is used, although frequency-dependent effects are typically observed in neuroscience experiments as in [59].

current. The I-V curve of the memristor as **c** 0.6 V sine input is applied with 0.25 V threshold and **d** 0.6 V triangle input applied with 0.5 V threshold, showing the characteristic decrease in pinched hysteresis lobe area as the frequency increases



**Fig. 4** State-altering and ionizing radiation effects on the memristive device. Input voltage ( $V_{mem}$ ) applied in **a**, **b** is a train of  $-500$  mV ( $40$  mV) pulses with duration  $150$  ms, which leads to decrease (increase) in synaptic weight of the device. When a state-altering radiation spike occurs,  $w/D$  sees a sudden undesirable

change increasing the conductivity and current within the device ( $I_{off}$ ) and circuit ( $I_{mem}$ ). On the other hand, when ionizing radiation spike occurs, it is compensated by a significant decrease in circuit current ( $I_{mem}$ ) without affecting the device synaptic state itself

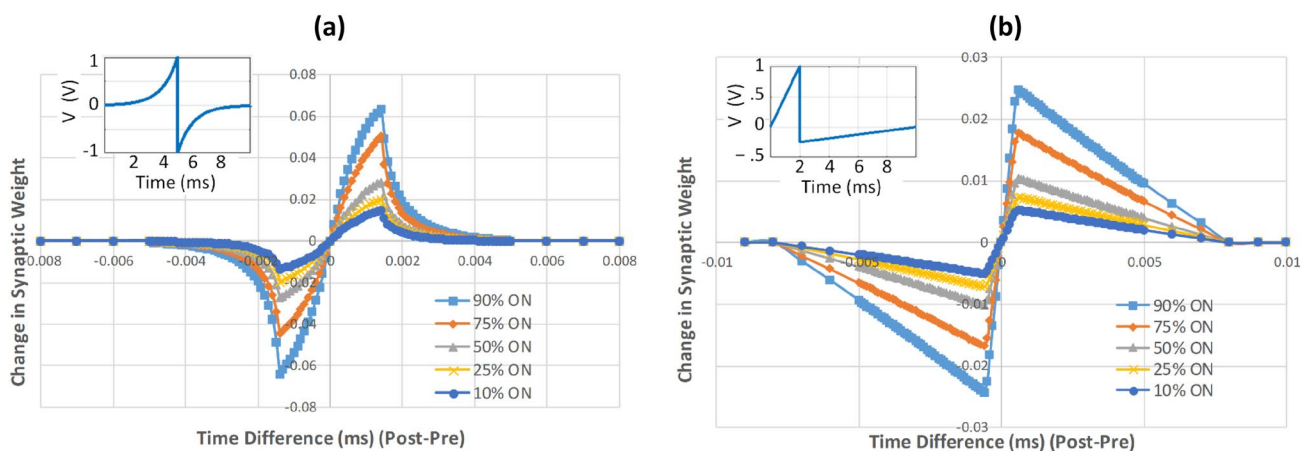
### 5.3.1 Effect of initial $w/D$

Different pre- and post-synaptic neuron spike shapes are used to obtain different STDP shapes using the given memristor model as shown in Fig. 5. STDP in Fig. 5a is obtained using exponential bi-phasic spikes and Fig. 5b used triangular bi-phasic spikes as shown in the respective insets. In Fig. 5, the magnitude of change in synaptic weight ( $\Delta w/D$ ) at any given time will depend on the initial synaptic state of the device. When the device was initially in a less conductive state (lower  $w/D$ , 10% on), about 6 to 10 times larger change in synaptic weight was observed

compared to if the device was initially at 90%  $w/D$ , i.e. in a highly conductive state. This was due to the non-linearity present in the device as discussed in Sect. 4.1.

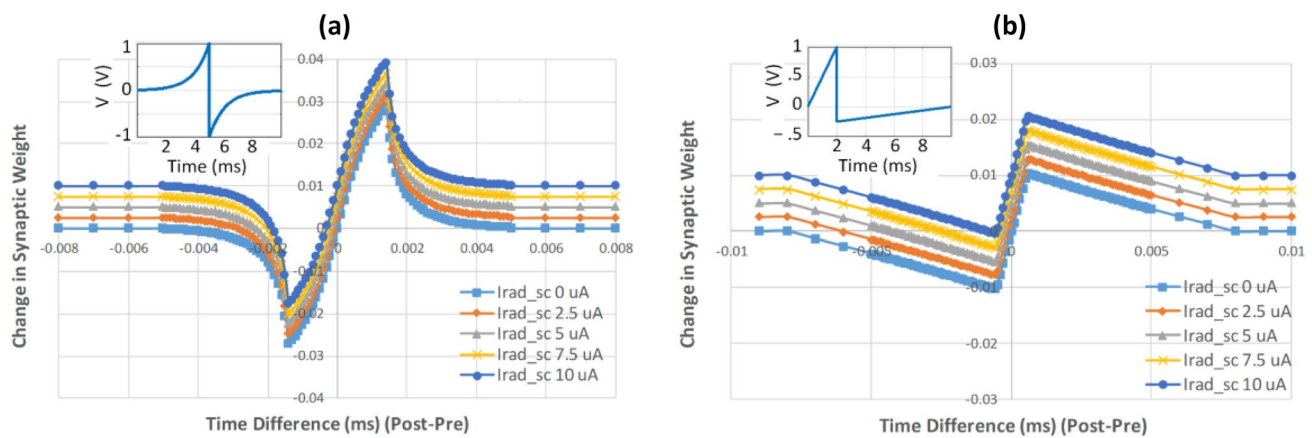
### 5.3.2 Effect of radiation

Figure 6 shows the change in STDP learning curve as the memristive device is exposed to a state-altering radiation event before pre- and post-synaptic afferent biphasic pulses arrive. Figure 6a shows the STDP curve resulting from the exponential bi-phasic spike and Fig. 6b resulted from triangular bi-phasic spike as shown in the respective



**Fig. 5** Different STDP shapes obtained using **a** exponential and **b** triangular bi-phasic pulses. The magnitude of change in synaptic weight ( $w/D$ ) also increases if the device was initially in the lower conductive state that is due to the non-linearity of the memristor model





**Fig. 6** STDP plot after a state-altering radiation event for **a** exponential and **b** triangular bi-phasic pulses. STDP curve shifts upward due to radiation that brings asymmetry in the STDP curve and thus tends to favor an increase in synaptic weight

insets. Radiation is observed to shift the whole curve upward making it asymmetric. Thus, learning will undesirably favor a stronger correlation and this could potentially make the system unstable. Unfortunately, unless the radiation is perfectly consistent, the action potential signals cannot be engineered to mitigate this asymmetry because doing so changes the shape of the STDP curve and affects the learning capability of the network.

#### 5.4 Radiation effects in the absence of patterns

Figure 7 represents the simulation results obtained using the fully connected pulsed neural network shown in Fig. 1a. Each afferent in the network generates a train of 500 mV (1 ms) square pulses at Poisson distributed inter-spike intervals representing pure noise (no patterns or correlations). The system is irradiated for the first 10 s with state-altering radiation of different magnitude

( $\mu = 1 \mu\text{A}$  to  $100 \mu\text{A}$  and  $\sigma = 0.5 \mu\text{A}$  to  $50 \mu\text{A}$ ) and flux up to  $5 \times 10^{10} \text{ cm}^{-2} \text{ s}^{-1}$ . Figure 7 plots w/D of each memristor ( $M_1$  to  $M_6$ ) after 50 s of simulation. Although the system is irradiated only for the first 10 s, radiation effects accumulate over time and at higher radiation intensity, the weights have considerably diverted. Some will even saturate, as is the case of  $M_4$ ,  $M_5$ , and  $M_6$  at the higher flux of  $5 \times 10^{10} \text{ cm}^{-2} \text{ s}^{-1}$ . This could lead to pattern learning and recognition challenges in neural networks. Additional results obtained using the pulsed neural network can be found in [44].

In this case, the network is exposed to radiation after already learning the pattern and is seeing random noisy input. It is observed that in the presence of radiation, synaptic weights drift away from the desired weight distribution, disrupting the pattern recognition capability of network. On the other hand, if the network is in

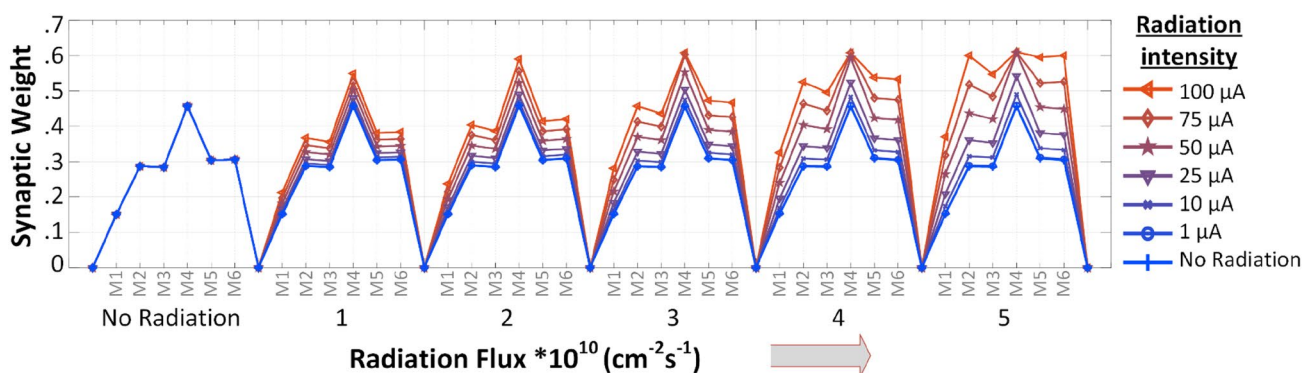


**Fig. 7** Synaptic weight (w/D) of memristor ( $M_1$  to  $M_5$ ) of the fully connected pulsed neural network represented in Fig. 1a source not found. **a** The network is simulated using 0.5 V, 1 ms square pulses, radiated for 10 s with state-altering radiation of different mean

magnitude and flux and w/D values are noted after 50 s of simulation. Radiation effects seem to cumulate over time, especially from stronger radiation events

learning and evolving its state, it is able to recover from the disturbances caused by the radiation events.

### 5.5 Pattern learning

Pre-synaptic afferents ( $N_1$  to  $N_{25}$  or  $100$ ) in the bi-phasic spiking neural network of Fig. 1b are firing at an average rate of 5 Hz for the 100 s simulation time. Afferents that are part of the pattern (a 10-pixel 'B') as shown by Fig. 8b (light color) are firing mutually correlated spikes at regular interval as shown in Fig. 8a,  $N_{12}$  and  $N_{13}$  [60, 61]. Conversely, non-participating afferents Fig. 8b (dark color) fire uncorrelated spikes with Poisson distributed intervals as shown by Fig. 8a  $N_{14}$  and  $N_{15}$ . This same firing pattern is used in generating 100-pixel 'B' patterns in larger 100 afferent networks of the next section. Pre- and post-synaptic afferents fire a biphasic triangular spike for 10 ms, which potentiates to a peak voltage of +1 V and depression tail reaches a max of  $-0.25$  V as shown in the inset in Fig. 9. All the memristors in the spiking neural networks are initially kept in a conductive state with resistance distribution varying from 20 k $\Omega$  and 35 k $\Omega$  as can be noted in Fig. 8b (Initial State). For training and testing purposes, the networks use biphasic triangular spikes as the learning and synaptic weight change evolution was linear. Linear learning is presented by the STDP learning curve in Fig. 6. Note that 25 or 100 correlated and uncorrelated afferents are arranged such that the data set represents the letter "B". Active afferents that are part of the pattern in letter "B" fire mutually correlated spikes, unlike, non-participating afferents that fire Poisson distributed uncorrelated spikes as shown in Fig. 8a.

Figure 8b shows the synaptic weight evolution of all the memristors ( $M_1$  to  $M_{25}$ ) as the network tries to learn the 25-pixel pattern representing a letter 'B'. Starting around 30 s, the network was able to depress most of the uncorrelated neurons by decreasing the conductivity of their corresponding memristors and the desired pattern is very recognizable. At 60 s, the network is in a stable state with post-synaptic neuron firing at a constant rate

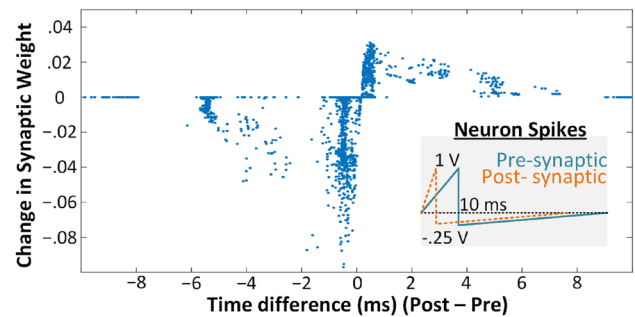


**Fig. 9** STDP plot obtained from weight changes due to nearest-neighbor pairs in the 100 s simulation of the network with 25 pre-synaptic bi-phasic spiking neurons of Fig. 1Err or ! Reference source not found.(b). Inset shows the pre- and post-synaptic neuron inputs used. STDP has much stronger depression than potentiation, generally leading to faster learning in the network

as the un-correlated neurons are completely depressed and thus not contributing any current to LIF circuit of the post-synaptic neuron. Figure 8c shows the synaptic weight distribution of the memristor and decrease in weight of uncorrelated synapses can be clearly noted at 30 s. In the following simulations, the input signals of 100 (or 25) pre-synaptic neurons were the same, and only the state-altering radiation flux and magnitude were changed.

The STDP learning curve in Fig. 9 shows changes in the synaptic weights of all 25 memristors over a period of 100 s as a function of the time difference between post- and pre-synaptic spike firing. When a post-synaptic neuron fires after a pre-synaptic neuron (time difference  $> 0$  ms), the network considers them correlated and the synaptic weight of the respective memristor increases making the synaptic connection more conductive (and vice-versa). The STDP curve shows much strong depression than potentiation, meaning the network is able to depress the uncorrelated afferents faster. Asymmetrical STDP curves are obtained using different potentiation for pre- and post-synaptic spike as shown in the inset in Fig. 9. More simulations of the 25-pixel network can be found in refs. [62] and [63].

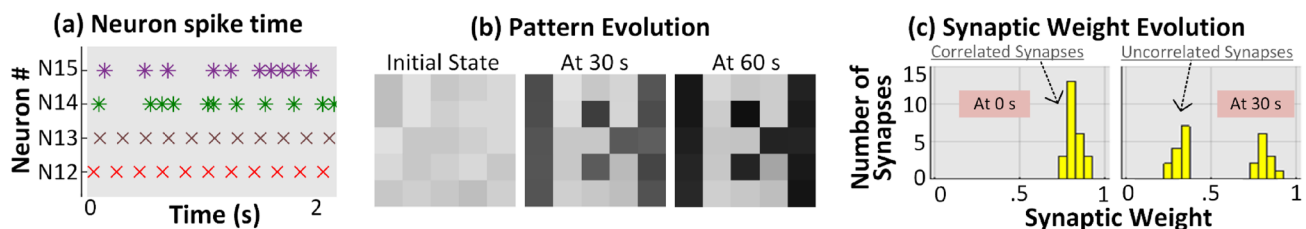


**Fig. 8** **a** Scatter plot of the spike times of two correlated afferents  $N_{12}$  and  $N_{13}$  (participating in the pattern) and two non-participating, uncorrelated afferents ( $N_{14}$  and  $N_{15}$ ). **b** The initial synaptic weight distribution and evolution of the pattern over time as the

system is in the process of learning 25-pixel letter 'B'. **c** A histogram of the synaptic weight distributions in weight bins that are 0.05 wide. After 30 s, uncorrelated neurons are separated and moved to lower weight

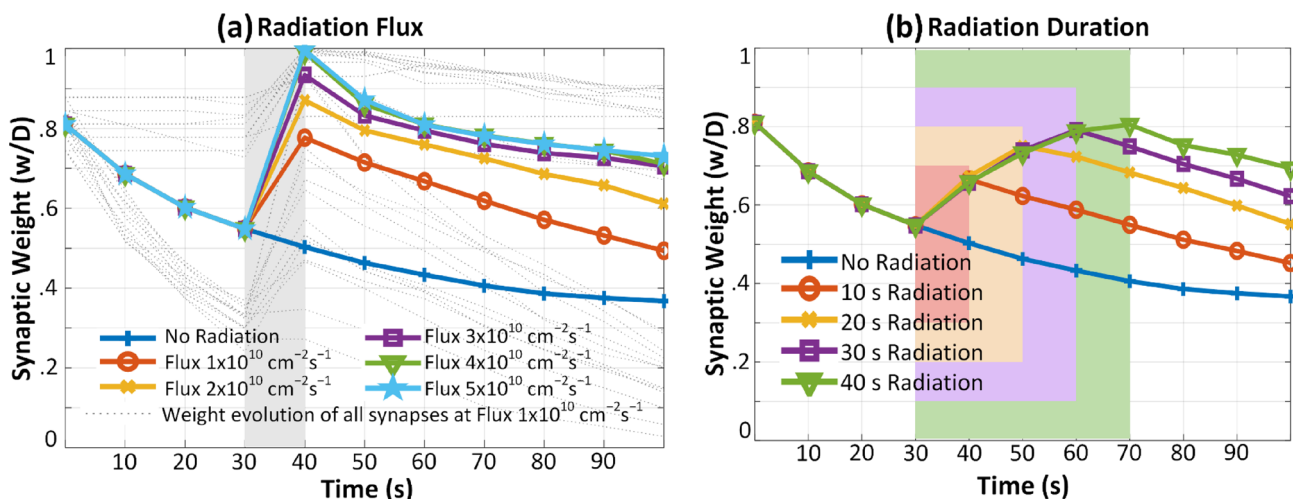
## 5.6 Pattern learning subject to radiation with limited duration

Figure 10 plots the evolution of all 25 memristors in biphasic spiking neural network in presence of state-altering radiation as the network is in the process of learning 25-pixel spatio-temporal pattern. In Fig. 10a, s of radiation exposure (grey area) starts at 30 s at mean magnitude  $\mu = 25 \mu\text{A}$  and  $\sigma = 12.5 \mu\text{A}$ , dotted grey lines represent the weight evolution of all 25 synapses at  $1 \times 10^{10} \text{ cm}^{-2} \text{ s}^{-1}$  flux. In Fig. 10b, the network is irradiated for a longer period of time up to 40 s (colored region), but at the lower magnitude of  $\mu = 5 \mu\text{A}$  and  $\sigma = 2.5 \mu\text{A}$ , each at  $3 \times 10^{10} \text{ cm}^{-2} \text{ s}^{-1}$  flux. In both the cases, after irradiation ceases, the mean synaptic weight tends to evolve toward the control trace (with no radiation). It is notable that in Fig. 10b, 40 s of irradiation does not saturate the average weight as it does in Fig. 10a where the radiation exposure only lasted 10 s.

Figure 11 shows the synaptic weight distribution and pattern evolution, as the spiking neural network is the process of learning a 100-pixel spatio-temporal pattern letter 'B'. Again, the network is exposed to 10 s of state-altering radiation (magnitude  $\mu = 25 \mu\text{A}$  and  $\sigma = 12.5 \mu\text{A}$ , starting at 30 s) at increasing flux. It is observed that as the flux increases, the pattern distortion also increases. This is because radiation is changing the state of the memristive synaptic devices and forcing them to be more conductive as indicated from the STDP curves in Sect. 4.3.2. As the weights move toward more conductive states, the LIF post-synaptic neuron observes stronger correlation and the system becomes unstable. For a neural network to be stable, synaptic weight distributions should look more like Fig. 8b at 30 s or 11a at 100 s,

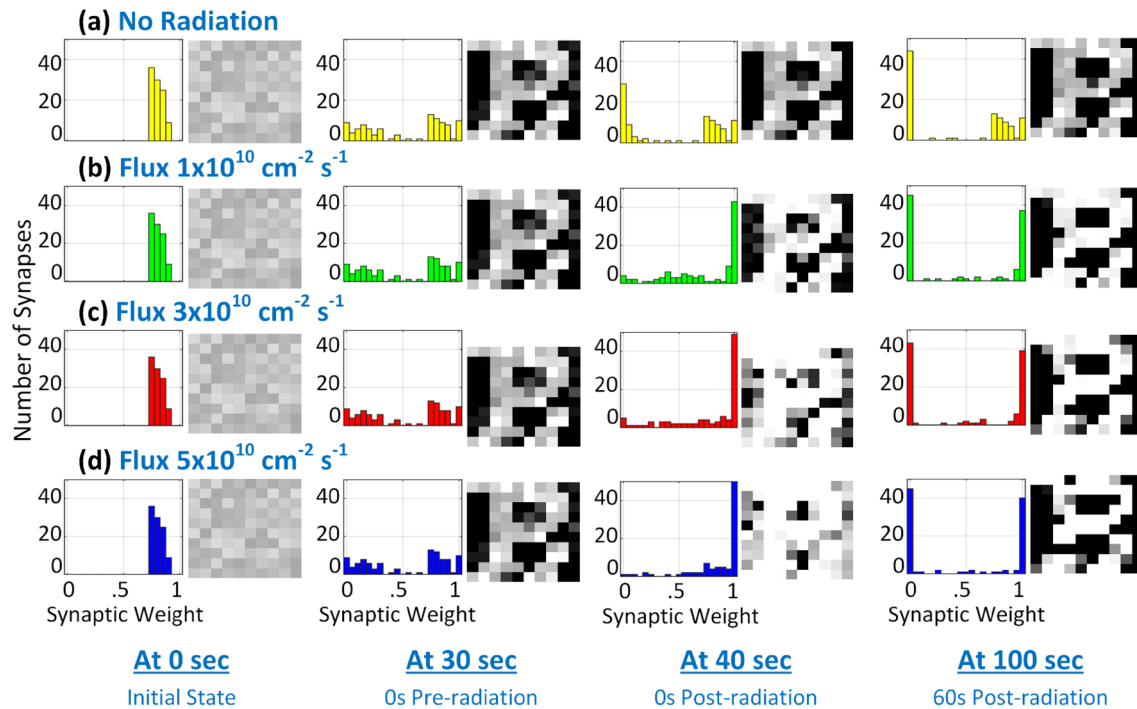
where correlated weights are not completely saturated and therefore not over-saturating the LIF post-synaptic neurons, but are contributing to the pattern. After the end of the 10 s state-change radiation event, the system tries to relearn the pattern but recovery does not necessarily result in the same pattern or a stable system. In the case of Fig. 11 at  $5 \times 10^{10} \text{ cm}^{-2} \text{ s}^{-1}$  flux, the pattern is indistinguishable at 40 s. During the post-radiation period, the pattern is mostly recovered, but has lost several pixels that should be participating in the pattern (Fig. 11d at 100 s). The network essentially depressed those pixels to gain stability and balance following instability induced by the radiation exposure.

Figure 12 shows a detailed analysis of data obtained from the network simulation in Fig. 11. Figure 12(a) plots the average synaptic weight evolution of all correlated and uncorrelated synapses separately over the 100 s period. During the radiation event (highlighted by the salmon color), uncorrelated synapses saw more deviation than correlated synapses. This effect is due to the non-linearity of the device as discussed in Sect. 4.3.1 and Fig. 5. When it is less conductive, there is a larger change in synaptic weight compared to a highly conductive state. It is also observed that the system became stable only after the average weight of uncorrelated afferents slid lower than 0.1 w/D (note dashed vertical lines). Due to this, all the correlated synapses do not average out at the same value and result in a slightly different learned pattern as noted in Fig. 11 at 100 s. This observation is clearer in Fig. 12b where the cumulative variance in a change of synaptic weight of correlated synapses stabilized after vertical dashed lines confirming the system stability. As expected the cumulative variance in weight change is



**Fig. 10** Average synaptic weight evolution of all memristors as the system is in the process of learning spatio-temporal pattern letter 'B'. **a** Evolution as system is radiated for 10 s with state-altering radiation at different flux (magnitude  $\mu = 25 \mu\text{A}$  and  $\sigma = 12.5 \mu\text{A}$ ). **b** Evolution as system is radiated with state-altering radiation

( $3 \times 10^{10} \text{ cm}^{-2} \text{ s}^{-1}$  flux, magnitude  $\mu = 5 \mu\text{A}$  and  $\sigma = 2.5 \mu\text{A}$ ) time increasing from 10 to 40 s (colored area). In both the case after the end of the radiation event, average synaptic weight evolves towards the non-radiated weight curve, thus the network is trying to relearn the pattern



**Fig. 11** The synaptic weight distribution and pattern evolution over time as the system is exposed to 10 s (starting at 30 s) state-altering radiation (magnitude  $\mu=25 \mu\text{A}$  and  $\sigma=12.5 \mu\text{A}$ ) at increasing flux. Spiking neural network is the process of learning 100-pixel spatio-temporal pattern letter 'B'. As the flux increases, pattern

distortion also increases. At  $5 \times 10^{10} \text{ cm}^{-2} \text{ s}^{-1}$  flux, the pattern is completely indistinguishable at 40 s. Although the system tries to relearn the pattern after the end of radiation exposure, the recovery does not result in the same pattern or a stable system

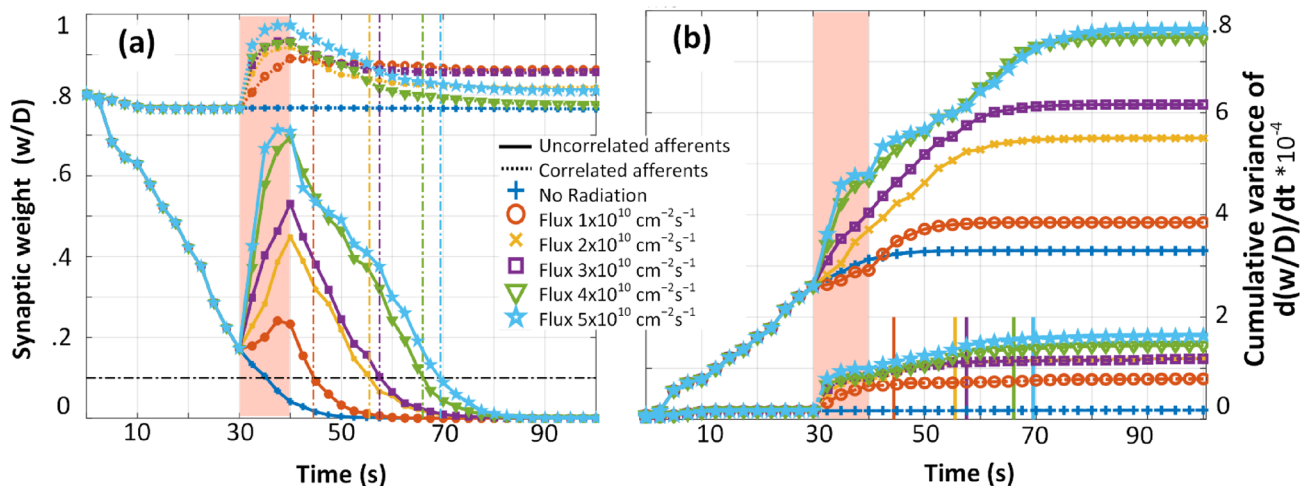


**Fig. 12** Network stability analysis of from the simulation in Fig. 11. **a** Average and **b** Cumulative variance in the change of synaptic weight evolution of all correlated and uncorrelated synapses over 100 s period. In **a** during the radiation event (salmon color), uncorrelated synapses saw more deviation than correlated synapses and

the system became stable only after the average weight of uncorrelated afferent slid lower than 0.1 w/D (dashed vertical lines). This observation can be made more clearly in **b** where the cumulative variance in synaptic weight of correlated synapses stabilized after the vertical dashed lines



higher for uncorrelated synapse and for higher flux. Formulas used in the calculations are given as:

$$\text{Average weight}(n) = \frac{1}{n} \sum_{i=1}^n ((w/D)_i)$$

$$\text{Cumulative Variance of } \frac{d(w)}{dt}(n) = \sum_{i=1}^n \left( \left( \frac{w}{D} \right)_i - (p)_i \right)^2$$

$$\text{Mean Squared Error (n)} = \frac{1}{n} \sum_{i=1}^n ((w/D)_i - (p)_i)^2$$

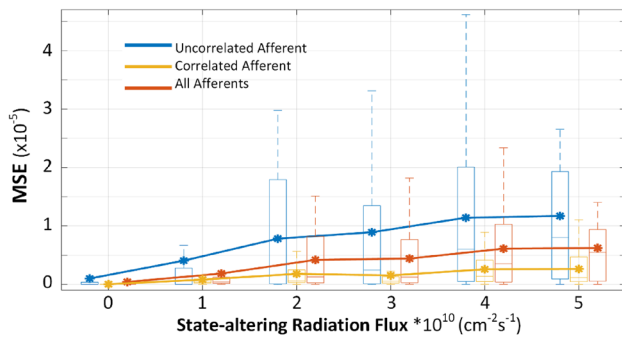


**Fig. 13** Error analysis of network from the simulation in Fig. 11. Box plot of mean squared error post-radiation (after 40 s) of uncorrelated, correlated and all synaptic weights. Note the increase in the average MSE and spread, as the radiation flux increases. Spread is more notable in uncorrelated synapses

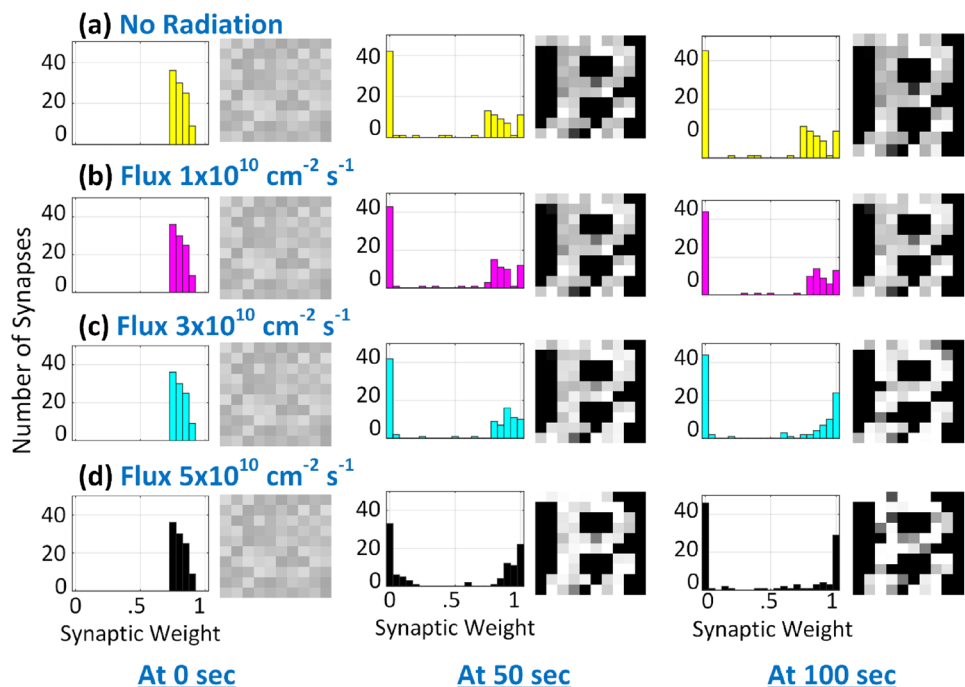
where  $n$  is the total number of synaptic memristor under analysis (uncorrelated, correlated or all) and  $p$  is the desired weight of the corresponding synaptic device.

A box plot of mean squared error (MSE) of post-radiation data (after 40 s) obtained from network simulation in Fig. 11 is plotted in Fig. 13 at different radiation flux for the synaptic weight of uncorrelated, correlated and all memristors ( $M_1$  to  $M_{100}$ ). As expected, the average MSE increases as the radiation increases and the box-whisker spread is significantly noticeable in the uncorrelated data set because it saw the most deviation during radiation as in Fig. 12a. It is notable that the median of radiated correlated data set is much closer to zero as this data set did not see much deviation during radiation due to STDP  $w/D$  non-linearity.

## 5.7 Pattern learning in the presence of constant radiation

Figure 14 shows the synaptic weight distribution and pattern evolution, as the spiking neural network is the process of learning the 100-pixel spatio-temporal pattern letter 'B'. The network is exposed to state-altering radiation (magnitude  $\mu = 0.5 \mu A$  and  $\sigma = 0.25 \mu A$ ) at increasing flux up to  $5 \times 10^{10} \text{ cm}^{-2} \text{ s}^{-1}$  throughout the learning process of 100 s. It can be noted in Fig. 14 at  $5 \times 10^{10} \text{ cm}^{-2} \text{ s}^{-1}$  flux at 100 s, correlated weights are pushed to the extreme. This again over-excites the LIF post-synaptic neuron and the system becomes unstable and does not recognize the expected pattern. On the other hand, at  $0.5 \times 10^{10} \text{ cm}^{-2} \text{ s}^{-1}$  flux, the

**Fig. 14** Synaptic weight distribution and pattern evolution over time as the system is exposed to state-altering radiation (magnitude  $\mu = 0.5 \mu A$  and  $\sigma = 0.25 \mu A$ ) at increasing flux throughout the learning process of 100 s. Spiking neural network is in the process of learning 100-pixel spatio-temporal pattern letter 'B'. As the flux increases, system instability increases but at lower flux, the system was able to maintain stability





system is very stable as the correlated weights are not saturated (LIF post-synaptic neuron is not over-stimulated) and the radiation is absorbed in the network.

Figure 15 shows the detailed analysis of data obtained from network simulation in Fig. 14. Figure 15a plots the average synaptic weight evolution of all correlated synapses over 100 s period. At higher radiation, a deflection point can be observed (represented by the dotted horizontal black line). As the average correlated synaptic weight evolves to this point, the system becomes unstable. This observation can also be verified when the cumulative variance in the change of synaptic weight of correlated afferent is plotted in Fig. 15a. Note that the cumulative

variance in weight keeps increasing after the deflection-point even though the system was relatively stable for flux  $3 \times 10^{10} \text{ cm}^{-2} \text{ s}^{-1}$  and  $4 \times 10^{10} \text{ cm}^{-2} \text{ s}^{-1}$  before deflection.

The MSE of w/D data obtained from network simulation in Fig. 14 is plotted in Fig. 16 at different radiation flux for synaptic weights of uncorrelated, correlated, and all memristors. Figure 16a plots the evolution of MSE over-time. As discussed in Sect. 4.5, all synapses are initialized to a fairly high conductance. Thus, uncorrelated synapses started with the most error (MSE = 0.7) and as the network suppressed them the MSE reduced to 0. On the other hand, correlated synapses started with nearly zero MSE that increased over time as the system depressed while

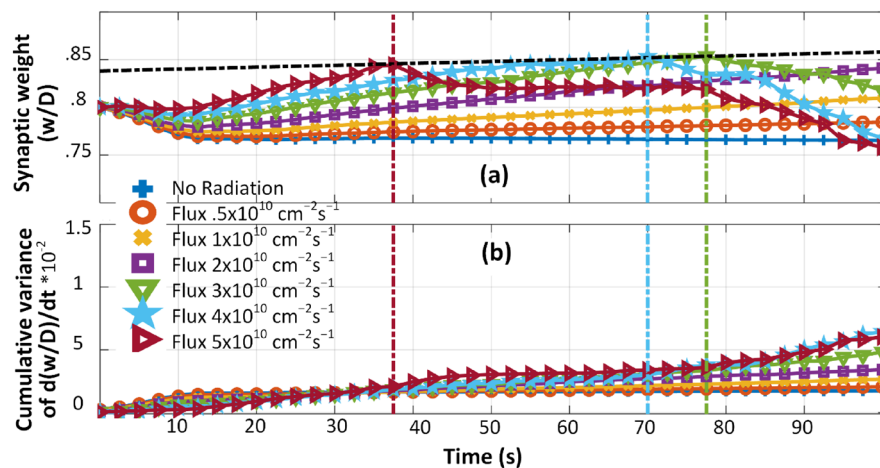


**Fig. 15** Stability analysis of network from the simulation in Fig. 14. **a** Average synaptic weight and **b** Cumulative variance in the change of synaptic weight of correlated synapses over 100 s period. In **a** at higher radiation deflection-point can be observed

represented by dotted horizontal black line system become unstable. This observation is clearer in **b** where the cumulative variance in weight of correlated synapses destabilizes after the vertical dashed lines representing the respective deflection-points

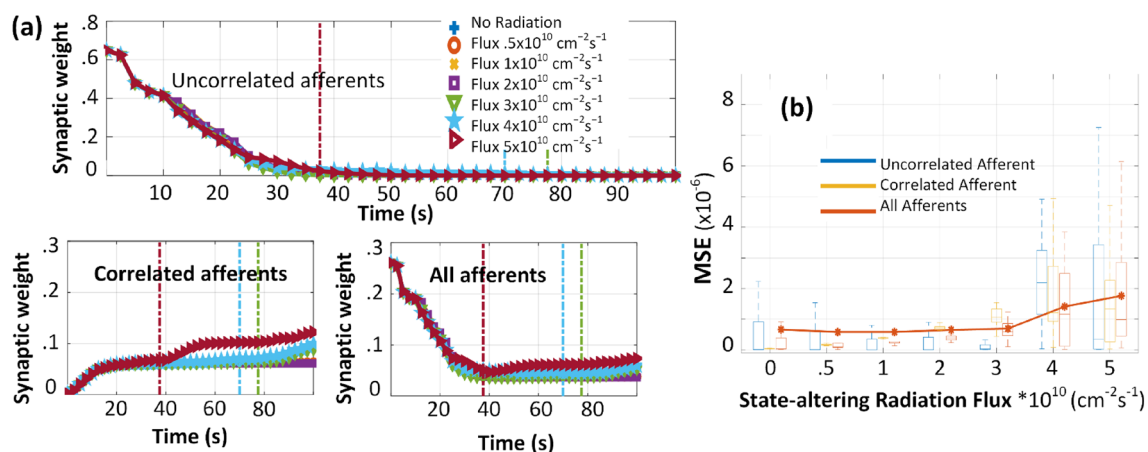


**Fig. 16** Error analysis of network from the simulation in Fig. 14. **a** MSE overtime and **b** Box plot of MSE for 100 s of uncorrelated, correlated and all synaptic weights. On average, MSE decreases at lower radiation flux in **a** but as radiation flux increases, correlated

synapses became unstable and MSE increases. Note the average MSE in **b** does not increase for lower flux and spread increases only at much higher radiation flux

potentiating a few of the correlated synapses to attain stability. On average, MSE decreased from 0.35 to 0.5 stably without or at lower radiation flux. On the other hand, as radiation flux increased, correlated synapses became unstable and MSE increased. Figure 16b compares the distribution of MSE as state-altering radiation flux increases from no radiation to  $5 \times 10^{10} \text{ cm}^{-2} \text{ s}^{-1}$ . As expected, the MSE increases as the radiation increases and box-whisker spread is significantly noticeable  $4 \times 10^{10} \text{ cm}^{-2} \text{ s}^{-1}$  and  $5 \times 10^{10} \text{ cm}^{-2} \text{ s}^{-1}$  as the system becomes more unstable due to weight saturation and LIF over-simulation. It is notable that the mean of radiated correlated data set is almost stable until  $3 \times 10^{10} \text{ cm}^{-2} \text{ s}^{-1}$  thus system was able to absorb the radiation for 100 s until that flux.

## 6 Conclusion

The effects of state-altering and ionizing radiation interaction events on the spatio-temporal pattern learning ability of memristor-based spiking neural networks are studied. Feed-forward neural networks are analyzed under irradiation at different flux, intensity, and duration as they are in the process of learning the 100- or 25-pixel character 'B'. A fully connected network is also analyzed for radiation effects in the absence of any pattern. Synaptic memristors in the networks use the STDP learning rule achieved using biphasic neural spikes to modify the conductivity between the two afferents. Effect of radiation events on STDP learning curves, pattern evolution, and synaptic weight evolution is analyzed throughout the paper. Network stability is subsequently compared by calculating cumulative variance in the change of synaptic weights and the mean-squared error (MSE).

It is observed that radiation events bring asymmetry to the STDP curve, artificially forcing the network to favor a stronger correlation between the afferents. If the network is exposed to higher state-altering radiation flux  $4 \times 10^{10} \text{ cm}^{-2} \text{ s}^{-1}$  or  $5 \times 10^{10} \text{ cm}^{-2} \text{ s}^{-1}$  for example) even for a shorter period such as 10 s, the network destabilizes and takes a relatively long time to stabilize and relearn the pattern. In such cases, the system might suppress a few of the correlated synapses thus resulting in a slightly different learned pattern. When exposed to smaller flux ( $1 \times 10^{10} \text{ cm}^{-2} \text{ s}^{-1}$ ), the system was very quickly (within 20 to 30 s) able to relearn the expected pattern and cope with the effect of radiation. In absence of a pattern (input is random Poisson noise), radiation effects accumulate over time and the network was never able to overcome them. At the same time, the system was able to learn and separate the uncorrelated afferents when a pattern was presented but the network was subjected to state-altering radiation at low flux.

To conclude, radiation does affect the learning capability of the spiking neural networks, but the pattern deterioration is negligible and generally recoverable at lower radiation flux and intensity even for longer period of exposure. Although the networks used in this study contain only two layers and relatively few neurons, they are representative of portions of larger networks. Specifically, the results could have implications for the fault-tolerance and reliability of future hardware implementations of deep spiking neural networks. In particular, filtering and convolution layers may learn slightly different functions when exposed to radiation. However, since MSE on a single layer was not significant at lower flux, larger networks may be able to overcome such effects.

**Funding** Supported by the Defense Threat Reduction Agency (DTRA) Grant HDTRA1-17-1-0036.

**Availability of data and materials** Not Applicable.

**Declarations**

**Conflict of interest** On behalf of all authors, the corresponding author states that there is no conflict of interest.

**Code availability** Not Applicable.

**Open Access** This article is licensed under a Creative Commons Attribution 4.0 International License, which permits use, sharing, adaptation, distribution and reproduction in any medium or format, as long as you give appropriate credit to the original author(s) and the source, provide a link to the Creative Commons licence, and indicate if changes were made. The images or other third party material in this article are included in the article's Creative Commons licence, unless indicated otherwise in a credit line to the material. If material is not included in the article's Creative Commons licence and your intended use is not permitted by statutory regulation or exceeds the permitted use, you will need to obtain permission directly from the copyright holder. To view a copy of this licence, visit <http://creativecommons.org/licenses/by/4.0/>.

## References

1. Ji S, Xu W, Yang M, Yu K (Jan. 2013) 3D convolutional neural networks for human action recognition. *IEEE Trans Pattern Anal Mach Intell* 35(1):221–231. <https://doi.org/10.1109/TPAMI.2012.59>
2. Cireşan DC, Meier U, Gambardella LM, Schmidhuber J (Dec. 2010) Deep, big, simple neural nets for handwritten digit recognition. *Neural Comput* 22(12):3207–3220. [https://doi.org/10.1162/NECO\\_a\\_00052](https://doi.org/10.1162/NECO_a_00052)
3. Hinton G et al (Nov. 2012) Deep neural networks for acoustic modeling in speech recognition: the shared views of four research groups. *IEEE Signal Process Mag* 29(6):82–97. <https://doi.org/10.1109/MSP.2012.2205597>

4. Yetis Y, Kaplan H, Jamshidi M (2014) Stock market prediction by using artificial neural network. In: 2014 world automation congress (WAC). <https://doi.org/10.1109/WAC.2014.6936118>.
5. Bojarski M et al (2016) End to end learning for self-driving cars, Apr. 2016, [Online]. <https://arxiv.org/abs/1604.07316>.
6. V. S. Kumar, J. Prasad, V. L. Narasimhan, and S. Ravi, "Application of artificial neural networks for prediction of solar radiation for Botswana," in *2017 International Conference on Energy, Communication, Data Analytics and Soft Computing (ICECDS)*, Aug. 2017, 3493–3501, doi: <https://doi.org/10.1109/ICECDS.2017.8390110>.
7. Dmitriev A, Minaeva Y, Orlov Y, Persiantsev I, Suvorova A, Veselovsky I (1999) Artificial neural network applications to the space radiation environment modelling and forecasting. In: ESA workshop on space weather, pp 393–397.
8. Santosh TV, Vinod G, Saraf RK, Ghosh AK, Kushwaha HS (2007) Application of artificial neural networks to nuclear power plant transient diagnosis. *Reliab Eng Syst Saf* 92(10):1468–1472. <https://doi.org/10.1016/j.jress.2006.10.009>
9. Keys AS, Adams JH, Cressler JD, Darty RC, Johnson MA, Patrick MC (2008) High-performance, radiation-hardened electronics for space and lunar environments. *AIP Conf Proc* 969:749–756. <https://doi.org/10.1063/1.2845040>
10. Dodd PE, Shaneyfelt MR, Schwank JR, Felix JA (2010) Current and future challenges in radiation effects on CMOS electronics. *IEEE Trans Nucl Sci* 57(4 Part 1):1747–1763. <https://doi.org/10.1109/TNS.2010.2042613>
11. Zamarreño-Ramos C et al (2011) On spike-timing-dependent-plasticity, memristive devices, and building a self-learning visual cortex. *Front Neurosci* 5(26):1–22. <https://doi.org/10.3389/fnins.2011.00026>
12. Serrano-Gotarredona T, Masquelier T, Prodromakis T, Indiveri G, Linares-Barranco B (2013) STDP and STDP variations with memristors for spiking neuromorphic learning systems. *Front Neurosci* 7(2):1–15. <https://doi.org/10.3389/fnins.2013.00002>
13. Boybat I et al (2018) Neuromorphic computing with multi-memristive synapses. *Nat Commun* 9(1):1–12. <https://doi.org/10.1038/s41467-018-04933-y>
14. Wozniak S, Pantazi A, Leblebici Y, Eleftheriou E (2017) Neuro-morphic system with phase-change synapses for pattern learning and feature extraction. In: *International joint conference on neural networks (IJCNN)*, 2017, pp 3724–3732. <https://doi.org/10.1109/IJCNN.2017.7966325>.
15. Reza S, Ganjtabesh M, Thorpe SJ (2018) STDP-based spiking deep convolutional neural networks for object recognition. *Neural Netw* 99:56–67. <https://doi.org/10.1016/j.neunet.2017.12.005>
16. Du Nguyen HA, Yu J, Xie L, Taouil M, Hamdioui S, Fey D (2017) Memristive devices for computing: beyond CMOS and beyond von Neumann. In: *2017 IFIP/IEEE International Conference on Very Large Scale Integration (VLSI-SoC)*, Oct. 2017, 1–10. <https://doi.org/10.1109/VLSI-SoC.2017.8203479>.
17. Zidan MA, Chen A, Indiveri G, Lu WD (2017) Memristive computing devices and applications. *J Electroceramics* 39(1–4):4–20. <https://doi.org/10.1007/s10832-017-0103-0>
18. Jo SH, Chang T, Ebong I, Bhadviya BB, Mazumder P, Lu W (2010) Nanoscale memristor device as synapse in neuromorphic systems. *Nano Lett*. 10(4):1297–1301. <https://doi.org/10.1021/nl904092h>
19. Masquelier T, Guyonneau R, Thorpe SJ (2008) Spike timing dependent plasticity finds the start of repeating patterns in continuous spike trains. *PLoS ONE* 3:1
20. Waibel A, Hanazawa T, Hinton GE, Shikano K, Lang KJ (1989) Phoneme recognition using time-delay neural networks. *Acoust Speech Signal Process IEEE Trans* 37(3):328–339. <https://doi.org/10.1109/29.21701>
21. Rowley H, Baluja S, Kanade T (1996) Neural network-based face detection. *Proc IEEE Conf Comput Vis Pattern Recognit* 20(January):203–207. <https://doi.org/10.1109/34.655647>
22. LeCun Y et al (Dec. 1989) Backpropagation applied to handwritten zip code recognition. *Neural Comput* 1(4):541–551. <https://doi.org/10.1162/neco.1989.1.4.541>
23. Fierro R, Lewis FL (1998) Control of a nonholonomic mobile robot using neural networks. *IEEE Trans Neural Netw* 9(4):589–600. <https://doi.org/10.1109/72.701173>
24. Baptista D, Abreu S, Freitas F, Vasconcelos R, Morgado-Dias F (2013) A survey of software and hardware use in artificial neural networks. *Neural Comput Appl* 23(3):591–599. <https://doi.org/10.1007/s00521-013-1406-y>
25. Misra J, Saha I (Dec. 2010) Artificial neural networks in hardware: A survey of two decades of progress. *Neurocomputing* 74(1–3):239–255. <https://doi.org/10.1016/j.neucom.2010.03.021>
26. Adhikari SP, Yang C, Kim H, Chua LO (2012) Memristor bridge synapse-based neural network and its learning. *IEEE Trans Neural Networks Learn Syst* 23(9):1426–1435. <https://doi.org/10.1109/TNNLS.2012.2204770>
27. Laiho M, Lehtonen E, Russell AMT, Dudek P (2010) Memristive synapses are becoming reality. *The Neuromorphic Engineer*.
28. Yang JJ, Strukov DB, Stewart DR (Jan. 2013) Memristive devices for computing. *Nat Nanotechnol* 8(1):13–24. <https://doi.org/10.1038/nnan.2012.240>
29. Deionno E, Looper MD, Osborn JV, Barnaby HJ, Tong WM (2013) Radiation effects studies on thin film TiO2 memristor devices. In: *IEEE Aerospace Conference and Processing*, pp 1–8. <https://doi.org/10.1109/AERO.2013.6497378>.
30. Tong WM et al (2010) Radiation hardness of TiO2 memristive junctions. *IEEE Trans Nucl Sci* 57(3 Part 3):1640–1643. <https://doi.org/10.1109/TNS.2010.2045768>
31. Marinella MJ et al (2012) Initial assessment of the effects of radiation on the electrical characteristics of memristive memories. *Nucl Sci IEEE Trans* 59(6):2987–2994. <https://doi.org/10.1109/TNS.2012.2224377>
32. Barnaby HJ et al (2011) Impact of alpha particles on the electrical characteristics of TiO2 memristors. *IEEE Trans Nucl Sci* 58(6 Part 1):2838–2844. <https://doi.org/10.1109/TNS.2011.2168827>
33. Gonzalez-Velo Y, Barnaby HJ, Kozicki MN (2017) Review of radiation effects on ReRAM devices and technology. *Semicond Sci Technol* 32:8. <https://doi.org/10.1088/1361-6641/aa6124>
34. Deionno E, Looper MD, Osborn JV, Palko JW (2013) Displacement damage in Tio2 Memristor devices. *IEEE Trans Nucl Sci* 60(2):1379–1383. <https://doi.org/10.1109/TNS.2013.2249529>
35. McLain ML et al (2014) The susceptibility of TaOx-based memristors to high dose rate ionizing radiation and total ionizing dose. *IEEE Trans Nucl Sci* 61(6):2997–3004. <https://doi.org/10.1109/TNS.2014.2364521>
36. Taggart JL et al (2014) Ionizing radiation effects on nonvolatile memory properties of programmable metallization cells. *IEEE Trans Nucl Sci* 61(6):2985–2990. <https://doi.org/10.1109/TNS.2014.2362126>
37. Butcher B et al (2010) Proton-based total-dose irradiation effects on Cu/HfO2:Cu/Pt ReRAM devices. *Nanotechnology*. <https://doi.org/10.1088/0957-4484/21/47/475206>
38. McDonald NR, Pino RE, Rozwood PJ, Wysocki BT (2010) Analysis of dynamic linear and non-linear memristor device models for emerging neuromorphic computing hardware design. *IJCNN* 2010:1–5. <https://doi.org/10.1109/IJCNN.2010.5596664>
39. Abdalla H, Pickett MD (2011) SPICE modeling of memristors. In: *IEEE international symposium on circuits and systems (ISCAS)*, pp 1832–1835. <https://doi.org/10.1109/ISCAS.2011.5937942>.
40. Kvaterny S, Friedman EG, Kolodny A, Weiser UC (2013) TEAM: threshold adaptive memristor model. *IEEE Trans Circuits Syst*

- I Regul Pap 60(1):211–221. <https://doi.org/10.1109/TCSI.2012.2215714>
41. Yakopcic C, Taha TM, Subramanyam G, Pino RE (2013) Generalized memristive device SPICE model and its application in circuit design. *IEEE Trans Comput Des Integr Circuits Syst* 32(8):1201–1214. <https://doi.org/10.1109/TCAD.2013.2252057>
  42. Yakopcic C et al (2011) A memristor device model. *Electron Device Lett* 32(10):1436–1438. <https://doi.org/10.1109/LED.2011.2163292>
  43. Kolka Z, Biolkova V, Bielek D (2015) Simplified SPICE model of TiO<sub>2</sub> memristor. In: 2015 international conference on memristive systems (MEMRISYS), Nov. 2015, 3, 1–2. <https://doi.org/10.1109/MEMRISYS.2015.7378384>
  44. Dahl SG, Ivans R, Cantley KD (2018) Modeling memristor radiation interaction events and the effect on neuromorphic learning circuits. In: Proceedings of the international conference neuromorphic system - ICONS '18, 1–8, 2018. <https://doi.org/10.1145/3229884.3229885>
  45. Taggart JL et al. (2016) Effects of 14 MeV neutron irradiation on the DC characteristics of CBRAM cells. In: 2016 16th European conference on radiation and its effective components system, 1–4, Sep. 2016. <https://doi.org/10.1109/RADECS.2016.8093120>
  46. Strukov DB, Snider GS, Stewart DR, Williams RS (2008) The missing memristor found. *Nature* 453:80–83. <https://doi.org/10.1038/nature06932>
  47. Joglekar YN, Wolf SJ (2009) The elusive memristor: Properties of basic electrical circuits. *Eur J Phys* 30(4):661–675. <https://doi.org/10.1088/0143-0807/30/4/001>
  48. Narasimham B et al (Dec. 2007) Characterization of digital single event transient pulse-widths in 130-nm and 90-nm CMOS technologies. *IEEE Trans Nucl Sci* 54(6):2506–2511. <https://doi.org/10.1109/TNS.2007.910125>
  49. Prinzie J, Steyaert M, Leroux P (2018) Radiation Effects in CMOS Technology.
  50. Lacoë RC (Aug. 2008) Improving integrated circuit performance through the application of hardness-by-design methodology. *IEEE Trans Nucl Sci* 55(4):1903–1925. <https://doi.org/10.1109/TNS.2008.2000480>
  51. Schwank JR et al (Aug. 2008) Radiation effects in MOS oxides. *IEEE Trans Nucl Sci* 55(4):1833–1853. <https://doi.org/10.1109/TNS.2008.2001040>
  52. Scarpa A, Paccagnella A, Montera F, Ghibaudo G, Pananakakis G (1997) Ionizing radiation induced leakage current on ultra-thin gate oxides. *IEEE Trans. Nucl. Sci.* 44(6 Part 1):1818–1825. <https://doi.org/10.1109/23.658948>
  53. Bôas ACV, Guazzelli MA, Giacomini RC, Medina NH (2019) Ionizing radiation effects in a rectifier circuit. *J Phys Conf Ser* 1291:1. <https://doi.org/10.1088/1742-6596/1291/1/012019>
  54. Alexander DR (2003) Transient ionizing radiation effects in devices and circuits. *IEEE Trans Nucl Sci* 50(3):565–582. <https://doi.org/10.1109/TNS.2003.813136>
  55. Chua L (2014) If it's pinched it's a memristor. *Memristors Memristive Syst* 9781461490:17–90. [https://doi.org/10.1007/978-1-4614-9068-5\\_2](https://doi.org/10.1007/978-1-4614-9068-5_2)
  56. Abbott LF, Nelson SB (2000) Synaptic plasticity: taming the beast. *Nat Neurosci* 3:1178–1183. <https://doi.org/10.1038/81453>
  57. Bi G, Poo M (2001) Synaptic modification by correlated activity: Hebb's postulate revisited. *Annu Rev Neurosci* 24:139–166. <https://doi.org/10.1146/annurev.neuro.24.1.139>
  58. Panwar N, Rajendran B, Ganguly U (2017) Arbitrary spike time dependent plasticity (STDP) in memristor by analog waveform engineering. *IEEE Electron Device Lett* 38(6):740–743. <https://doi.org/10.1109/LED.2017.2696023>
  59. Lisman J, Spruston N (2010) Questions about STDP as a general model of synaptic plasticity. *Front Synaptic Neurosci* 2:140. <https://doi.org/10.3389/fnsyn.2010.00140>
  60. Ivans RC, Cantley KD, Vogel EM, Ivans RC, Subramaniam A, Vogel EM (2017) Spatio-temporal pattern recognition in neural circuits with memory-transistor-driven memristive synapses. *IJCNN* 2017:4633–4640. <https://doi.org/10.1109/IJCNN.2017.7966444>
  61. Wozniak S, Tuma T, Pantazi A, Eleftheriou E (2016) Learning spatio-temporal patterns in the presence of input noise using phase-change memristors. In: Proceedings of the IEEE international symposium on circuits system, 2016-July, 365–368, May 2016. <https://doi.org/10.1109/ISCAS.2016.7527246>
  62. Dahl SG, Ivans RC, Cantley KD (2019) Radiation effect on learning behavior in memristor-based neuromorphic circuit. In: 2019 IEEE 62nd international midwest symposium on circuits and systems (MWSCAS), 2019, 53–56. <https://doi.org/10.1109/MWSCAS.2019.8885288>
  63. Dahl SG, Ivans RC, Cantley KD (2019) Learning behavior of memristor-based neuromorphic circuits in the presence of radiation. *Proc Int Conf Neuromorph Syst.* <https://doi.org/10.1145/3354265.3354272>

**Publisher's Note** Springer Nature remains neutral with regard to jurisdictional claims in published maps and institutional affiliations.